



Deformation of NaCoF₃ perovskite and post-perovskite up to 30 GPa and 1013 K: implications for plastic deformation and transformation mechanism

Jeffrey P. Gay¹, Lowell Miyagi², Samantha Couper², Christopher Langrand¹, David P. Dobson³, Hanns-Peter Liermann⁴, and Sébastien Merkel¹

¹Univ. Lille, CNRS, INRA, ENSCL, UMR 8207 - UMET - Unité Matériaux et Transformations, 59000 Lille, France

²Department of Geology and Geophysics, University of Utah, Salt Lake City, UT 84108, USA

³Department of Earth Sciences, University College London, Gower Street, London WC1E 6BT, UK

⁴Deutsches Elektronen-Synchrotron (DESY), 22607 Hamburg, Germany

Correspondence: Jeffrey P. Gay (jeffrey-phillip.gay@univ-lille.fr) and Sébastien Merkel (sebastien.merkel@univ-lille.fr)

Received: 11 May 2021 – Revised: 9 August 2021 – Accepted: 19 August 2021 – Published: 30 September 2021

Abstract. Texture, plastic deformation, and phase transformation mechanisms in perovskite and post-perovskite are of general interest for our understanding of the Earth's mantle. Here, the perovskite analogue NaCoF₃ is deformed in a resistive-heated diamond anvil cell (DAC) up to 30 GPa and 1013 K. The in situ state of the sample, including crystal structure, stress, and texture, is monitored using X-ray diffraction. A phase transformation from a perovskite to a post-perovskite structure is observed between 20.1 and 26.1 GPa. Normalized stress drops by a factor of 3 during transformation as a result of transient weakening during the transformation. The perovskite phase initially develops a texture with a maximum at 100 and a strong 010 minimum in the inverse pole figure of the compression direction. Additionally, a secondary weaker 001 maximum is observed later during compression. Texture simulations indicate that the initial deformation of perovskite requires slip along (100) planes with significant contributions of {110} twins. Following the phase transition to post-perovskite, we observe a 010 maximum, which later evolves with compression. The transformation follows orientation relationships previously suggested where the *c* axis is preserved between phases and *hh0* vectors in reciprocal space of post-perovskite are parallel to [010] in perovskite, which indicates a martensitic-like transition mechanism. A comparison between past experiments on bridgmanite and current results indicates that NaCoF₃ is a good analogue to understand the development of microstructures within the Earth's mantle.

1 Introduction

Earth's lower mantle is believed to be composed predominantly of bridgmanite, i.e., (Mg,Fe)SiO₃ in the perovskite structure (Tschauner et al., 2014). At deep-lower-mantle conditions, this composition transforms from the perovskite to the post-perovskite structure (Murakami et al., 2004; Oganov and Ono, 2004). The deformation and transformation of perovskite and post-perovskite phases are important for a number of processes in the deep Earth (Čížková et al., 2010; Nakagawa and Tackley, 2011; Tackley, 2012), including the

development of crystallographic preferred orientation (Yamazaki and Karato, 2007; McCormack et al., 2011; Hunt et al., 2016), also known as texture, which can lead to seismic anisotropy (Cobden et al., 2015; Walker et al., 2018b). Texture development can also be studied experimentally (Wenk et al., 2006; Merkel et al., 2007; Miyagi et al., 2010) and is thought to be a reasonable approximation for seismic anisotropy observed within the mantle (Wookey et al., 2002; Nowacki et al., 2010; Ferreira et al., 2019).

Seismic anisotropy within the Earth's deep mantle is commonly measured using shear wave splitting. This shear wave

splitting can be used to characterize mantle strain fields, which in turn allows for mantle structures to be observed (Savage, 1999). There are many regions within the lower mantle, past 1000 km, that are seismically isotropic (Panning and Romanowicz, 2006; Beghein et al., 2006) even though numerous experimental studies demonstrate lower-mantle phases of bridgmanite and ferropericlase are highly anisotropic and even increase in anisotropy with depth (Chen et al., 1998; Mainprice et al., 2000). In the case of the D'' region, where a phase transformation from perovskite to post-perovskite could take place (Murakami et al., 2004; Hernlund et al., 2005; Koelemeijer et al., 2018), strong anisotropy is observed (Garnero et al., 2004; Panning and Romanowicz, 2006; Wookey and Kendall, 2007). It is difficult, however, to determine the physical origin of anisotropy (i.e., crystallographic preferred orientation or periodic layering) due to poor azimuthal sampling of D'' (Romanowicz and Wenk, 2017). Recent studies (Nowacki et al., 2013; Koelemeijer et al., 2018; Pisconti et al., 2019) show that the effect of post-perovskite is observable in seismic data, but the details of the transformation between bridgmanite and post-perovskite have an impact on the observed data (Pisconti et al., 2019; Walker et al., 2018a) and require further experimental characterization. In order to characterize how bridgmanite and post-perovskite deform within the lower mantle and what mechanisms are responsible for the transformations of bridgmanite to post-perovskite, it is necessary to utilize experimental mineral physics.

The study of the transition of perovskite to post-perovskite requires the application of pressure (P). Several experimental methods can be used to study deformation and phase transformation in situ at high pressure, such as the diamond anvil cell (DAC) (Wenk et al., 2004b; Miyagi and Wenk, 2016), the multi-anvil press (Cordier et al., 2004; Walte et al., 2009; Wang et al., 2013; Tsujino et al., 2016; Hunt et al., 2016), and the rotational Drickamer apparatus (Girard et al., 2016). For many years, deformation experiments in the DAC were limited to ambient temperatures (T). Recent developments, however, allow for the combined application of pressure and temperatures up to 1900 K (Liermann et al., 2009; Miyagi et al., 2013; Immoor et al., 2020), which we will use here. In addition, structural analogues of (Mg,Fe)SiO₃ can undergo perovskite to post-perovskite phase transitions at lower pressures and temperatures, making quantitative deformation experiments less challenging. Several experiments on analogues have resulted in perovskite and/or post-perovskite deformation and transformation textures (Niwa et al., 2007; Okada et al., 2010; Dobson et al., 2011; Miyagi et al., 2011; Dobson et al., 2013). Furthermore, deformation experiments on analogues can be used to gain insight on the plasticity of perovskite phases and can be compared to the behavior of (Mg,Fe)SiO₃ at mantle conditions (e.g., Fig. 10 in Wang et al., 2013). Not all analogues behave in the same manner, however. Deformation textures in CaIrO₃ post-perovskite, for instance, are known to be different from those measured

in (Mg,Fe)SiO₃ or MgGeO₃ (Miyagi et al., 2008). Numerical modeling has also been implemented in order to investigate deformation mechanisms in perovskite and post-perovskite (e.g., Ferré et al., 2007; Carrez et al., 2007; Mainprice et al., 2008; Metsue et al., 2009; Boioli et al., 2017; Carrez et al., 2017). This allows for the study of not only the effect of chemistry, pressure, and temperature but also the effects of strain rate on perovskite and post-perovskite deformation, which can not be measured in experiments using current experimental techniques.

Questions remain regarding compression textures, deformation mechanisms, and phase transformation mechanisms in perovskites and post-perovskites. The comparison of NaCoF₃ to (Mg,Fe)SiO₃ in deformation experiments is essential in order to determine if NaCoF₃ is a relevant experimental analogue. Additionally, understanding how transformation mechanisms vary between analogues and natural compositions, including their effects on deformation and transformation textures, can inform us on the validity of analogues and their ability to predict the behavior of natural samples when direct studies of (Mg,Fe)SiO₃ cannot be performed. Here we use a resistive-heated radial DAC combined with synchrotron radiation at pressures and temperatures between 1.1 and 29.6 GPa and 300 and 1013 K, respectively, to observe in situ texture development and phase change from a perovskite to a post-perovskite structure in NaCoF₃. We use these data to model plastic deformation and deformation mechanisms in perovskite. We find (100) $\{011\}$ slip and $\{110\}\{1\bar{1}0\}$ twins to be the most active deformation mechanisms during initial deformation of the perovskite phase. Texture measurements in these experiments are used to model orientation relationships and transformation mechanisms between perovskites and post-perovskites. We determine that the transformation of NaCoF₃ perovskite to post-perovskite is martensitic in nature, with orientation relationships matching those of NaNiF₃ outlined in Dobson et al. (2013). Normalized stress measurements also demonstrate a stronger perovskite phase than post-perovskite phase in NaCoF₃. Overall, these results can help us to better understand the deformation and phase transformation in perovskite and post-perovskite phases and will lead to greater knowledge of deep mantle dynamics.

2 Experimental details

2.1 High- P - T experiments

In this study, we use a graphite resistive-heated radial DAC apparatus to perform a uniaxial compression experiment on a polycrystalline sample of NaCoF₃. Experiments were performed on beamline P02.2 of the PETRA III facility at the Deutsches Elektronen Synchrotron (DESY) in Hamburg, Germany. By utilizing synchrotron X-ray diffraction in radial geometry, the stress state and texture of the sample can

be analyzed in situ at high pressure and temperature. An incident monochromatic X-ray beam focused to $5.8\ \mu\text{m} \times 3.2\ \mu\text{m}$ and PerkinElmer XRD 1621 detector with $200\ \mu\text{m} \times 200\ \mu\text{m}$ pixel size were used to capture the diffraction images. A CeO₂ standard from the National Institute of Standards and Technology (NIST; 674b) was used for calibration in order to correct for detector tilt and calculate a sample to detector distance of 438.35 mm. Wavelength was fixed at 0.4908 Å.

Powdered NaCoF₃ perovskite from the study of Dobson et al. (2011) was loaded into an X-ray transparent boron epoxy gasket with an 80 μm diameter hole. A platinum flake was also loaded to be used as a pressure marker, using the thermal equation of state parameters of Zha et al. (2008) and the EosFit program (Gonzalez-Platas et al., 2016).

Details on the synchrotron beamline setup and DAC can be found in Liermann et al. (2015) and Immoor et al. (2020). The diamonds we used had a 300 μm culet size. Two thin graphite layers in contact with the anvils and surrounding the diamond tips were used for a resistive heater, while two type-R thermocouples were used to monitor temperature. One of the thermocouples is located between both graphite heaters and the second on the diamond anvil next to the culet. Reported temperatures are the average between both thermocouple measurements. The graphite sheets contained a small window that was carved out of the graphite in order to allow the X-rays to pass through the heater. The DAC assembly was placed within a vacuum chamber maintaining a pressure of 10^{-3} mbar in order to prevent oxidation during heating. A water cooling system kept at low temperatures was used to prevent the assembly from overheating. The sample was compressed using a gas membrane system, while radial diffraction images were simultaneously collected.

The sample was pre-compressed up to 3.4 GPa at ambient temperature to close the sample chamber. Temperature was then increased to 873 K over the course of 3 h. NaCoF₃ was compressed to a maximum pressure of 30.8 GPa and heated at temperatures ranging from 861 to 1013 K (Table 1, Fig. 1). Diamonds broke at 30.8 GPa, marking the end of the experiment. We observe the transformation of NaCoF₃ perovskite to a post-perovskite structure (e.g., Fig. 1) between 20.1 and 26.1 GPa. During the first stage of compression from 1.1 GPa to 14.8 GPa temperatures are held constant between 861 and 868 K. Thereafter, temperature is increased to 997 K at 20.1 GPa just before the transition. The post-perovskite phase is then visible in the diffraction pattern at 26.1 GPa and 1013 K, although some perovskite may still be visible. Data files used can be found online (Gay et al., 2021).

2.2 Data analysis

Diffraction images were integrated over 5° azimuthal arcs into 72 spectra and analyzed using the program MAUD (material analysis using diffraction) (Lutterotti et al., 1997) following the general refinement procedure outlined in Wenk et al. (2014). An example of MAUD refinement is shown in

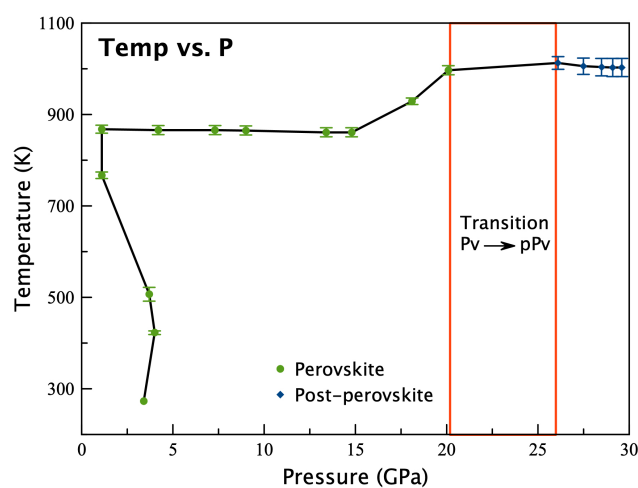


Figure 1. Pressure–temperature path during the experiment. Start of high-temperature compression is at 1.1 GPa and 868 K. Perovskite to post-perovskite transformation is observed between 20.1 and 26.1 GPa.

Fig. 2. Graphite peaks become more visible as pressure increases (e.g., Fig. 2b at 2θ values 6.0, 8.2, 13.4, and 14.6°). This is due to the closure of the window carved into the heater as the experiment proceeds. We exclude these regions in addition to the 2θ ranges where platinum is overlapping during the refinement process.

Diffraction background was fit using polynomial functions. Structural parameters of NaCoF₃ were obtained from Shirako et al. (2012), and cell parameters and B factors were further refined using the data. Crystallite size and microstrains were refined using the Popa line-broadening size-strain model (Popa, 1998).

Differential stress in NaCoF₃ was fit using a model that relies on the elastic theory of Singh et al. (1998), which assumes isotropic elastic properties and fits a value for the differential stress according to the displacement of peak positions with orientations. In the model of Singh et al. (1998), the average lattice strain across the sample is proportional to stress using $t = 6G\langle Q(hkl) \rangle$, where G is the shear modulus of the polycrystal sample and $\langle Q(hkl) \rangle$ is the average lattice strain across the sample. The MAUD fit requires an input value of the shear modulus, which is unknown for NaCoF₃ perovskite and post-perovskite at high temperature. In view of that limitation we use a constant value of $G = 44$ GPa, extracted from first-principles calculations on a cubic NaCoF₃ perovskite at zero pressure and temperature (Chenine et al., 2018). The t/G values are then recalculated from the fitted t and the fixed G values. Do note, however, the G value used when refining t in MAUD has no impact on the final t/G ratio. Also note that MAUD allows for extraction of individual $Q(hkl)$ for each diffraction peak, but the quality of our data and the number of overlapping peaks for perovskite and post-perovskite structures do not allow us to do so.

Table 1. Image number, pressure (P), temperature (T), lattice parameters, normalized stress, and crystallite size (CS) measured in the experiment. Numbers in parenthesis for temperatures are uncertainties on the last digits, determined from the difference in readings of both thermocouples. Errors are estimated to be 0.07 and 0.1 Å³ for perovskite and post-perovskite unit cell volumes, respectively, 0.002 Å for unit cell parameters, 0.0002 for normalized stresses, and approximately 200 Å³ for crystallite sizes. NaCoF₃ perovskite cell parameters are displayed in the Pbnm space group.

Image	P (GPa)	T (K)	Pt	NaCoF ₃					
				Phase	a (Å)	b (Å)	c (Å)	t/G	CS (Å)
3	3.4	301 (0)	3.907	Pv	5.297	5.580	7.694	0.028	277
7	4.0	423 (4)	3.906	Pv	5.293	5.570	7.681	0.039	286
12	3.7	507 (15)	3.907	Pv	5.305	5.560	7.678	0.039	249
17	1.1	767 (7)	3.920	Pv	5.392	5.588	7.774	0.029	272
38	1.1	868 (9)	3.918	Pv	5.363	5.553	7.720	0.010	465
46	4.2	866 (10)	3.907	Pv	5.302	5.526	7.653	0.022	475
52	7.3	866 (10)	3.893	Pv	5.227	5.503	7.592	0.037	428
57	9.0	865 (10)	3.886	Pv	5.162	5.488	7.547	0.041	388
66	13.4	861 (10)	3.868	Pv	5.034	5.468	7.469	0.049	337
69	14.8	861 (10)	3.863	Pv	4.995	5.467	7.444	0.051	231
73	18.1	929 (7)	3.852	Pv	4.921	5.456	7.391	0.054	143
77	20.1	997 (10)	3.844	Pv	4.852	5.485	7.339	0.048	104
79	26.1	1013 (14)	3.824	pPv	2.894	9.030	6.974	0.016	87
83	27.5	1006 (18)	3.819	pPv	2.884	9.022	6.950	0.018	100
86	28.5	1004 (19)	3.816	pPv	2.872	9.014	6.944	0.018	107
87	29.1	1003 (20)	3.814	pPv	2.868	9.012	6.935	0.018	171
88	29.6	1003 (20)	3.813	pPv	2.867	9.008	6.930	0.020	359

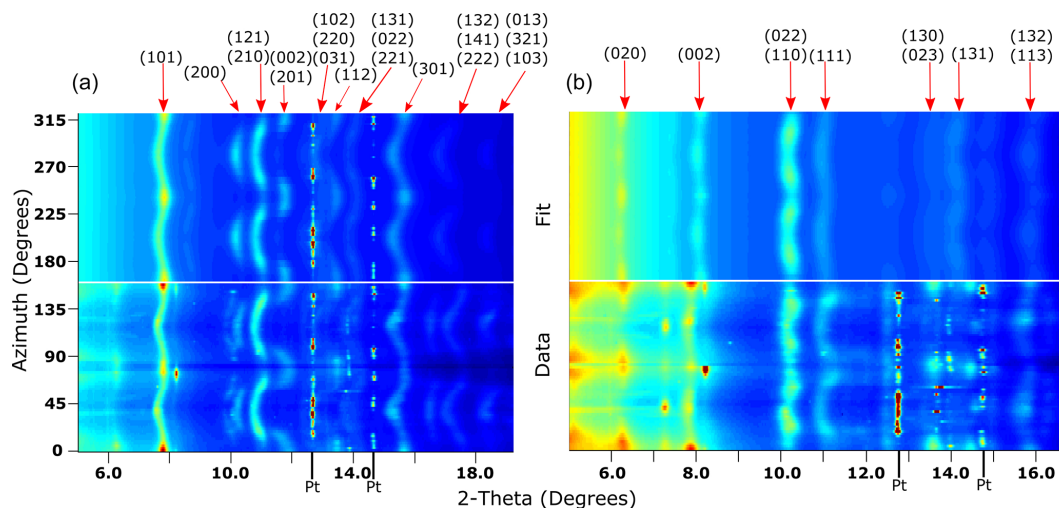


Figure 2. (a) Unrolled diffraction image of NaCoF₃ perovskite at 20.1 GPa and 997 K, immediately before transformation to post-perovskite. Below: measured diffraction (labeled data). Above: diffraction image recalculated by MAUD (labeled fit). Diffraction peaks of perovskite are labeled by their Miller indices, and platinum peaks are indicated by Pt. (b) Diffraction and fit for post-perovskite phase at 26.1 GPa and 1013 K. In both (a) and (b) diffraction lines vary in position and intensity, revealing texture and stress development due to compression. Graphite peaks from the heater are present at 6.0, 8.2, 13.4, and 14.6° 2 θ . These diffraction peaks, becoming more visible as the experiment proceeds, show no strain and were ignored if necessary during the refinement process.

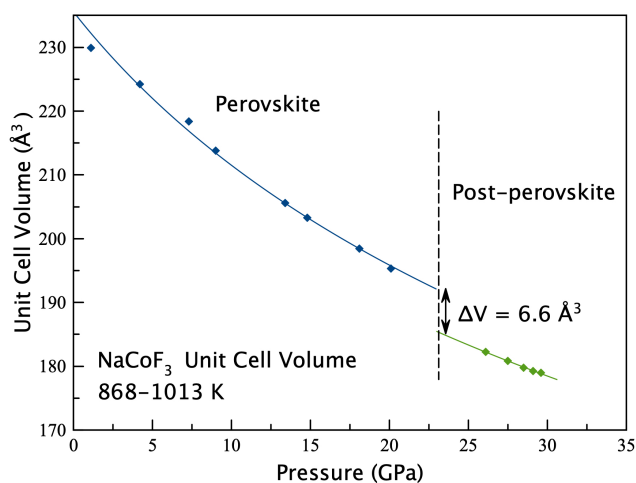


Figure 3. Unit cell volumes of NaCoF₃ perovskite and post-perovskite plotted vs. pressure. Lines are second-order Birch–Murnaghan equation of state, fit for each phase assuming constant temperature and used to illustrate compression behavior vs. experimental values.

Orientation distribution functions (ODFs) were calculated using the entropy Williams–Matthies–Imhof–Vinel (E-WIMV) algorithm which accounts for incomplete and arbitrary pole coverage. The ODF is a probability distribution function to find an orientation, which is normalized over the entire sample. An ODF with a multiple of random distribution (mrd) of 1 indicates a random orientation. Values greater or smaller than 1 indicate preferred orientation within an aggregate of grains, which we refer to as texture. Compression in the diamond anvil cell imposes a symmetry along the compression direction, set as the z axis in MAUD. Therefore, we impose a fiber symmetry and use an ODF resolution of 15°.

3 Results

NaCoF₃ crystallizes in the perovskite structure at ambient conditions. We observe a transformation to post-perovskite between 20.1 and 26.1 GPa at temperatures of ≈ 1000 K.

Unit cell volumes of NaCoF₃ in perovskite and post-perovskite are shown in Fig. 3 and the corresponding unit cell parameters in Table 1. In this study, we use the Pbnm space group for the orthorhombic setting of the perovskite phase. MAUD does report errors for each of the fitted parameters; however, these values underestimate the true physical error of the measurement. Hence, errors for unit cell volumes, unit cell parameters, normalized stress, and crystallite size have been estimated by running multiple series of MAUD refinements from different starting values. The error values reported in the caption of Table 1 are the maximum variation of each quantity. We observe a smooth decrease in unit cell volume with pressure.

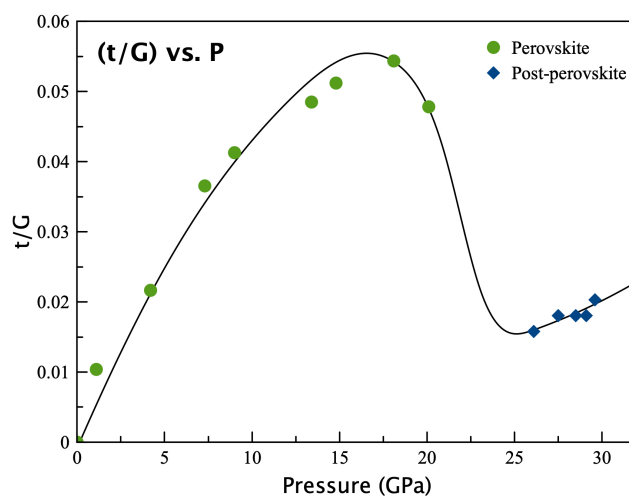


Figure 4. Normalized stress t/G in NaCoF₃ perovskite (green circles) and post-perovskite (blue diamonds) as a function of pressure. The solid line is a visual guide through the experimental data. The perovskite to post-perovskite transition occurs between 20.1 and 26.1 GPa.

We used the program EosFit (Gonzalez-Platas et al., 2016) to fit a second-order Birch–Murnaghan equation of state trend for perovskite between 1.1 GPa and 868 K and 20.1 GPa and 997 K and for all post-perovskite data. Considering the small ranges in temperature for the measurements, temperature effects were ignored. The resulting bulk modulus for perovskite and post-perovskite in the 868–1013 K range are 74.9 and 85.9 GPa, respectively. Based on Fig. 3, the drop of volume at the perovskite to post-perovskite transition is estimated to be 6.6 Å³.

Since the pressure and temperature effect on shear modulus is unknown for NaCoF₃, we report stresses in terms of normalized stress t/G . This quantity is a more appropriate representation of stress, does not require the extrapolation of G , and has been used in past studies to compare materials to each other (Duffy, 2007; Miyagi et al., 2009; Dorfman et al., 2015). As pressure increases from 1.1 to 18.1 GPa at temperatures between 868 and 929 K, normalized stress in NaCoF₃ perovskite increases from 0.010 to 0.054 (Fig. 4). Before the onset of transformation to post-perovskite, we observe a decrease in normalized stress to 0.048 at 997 K. This decrease in stress is likely due to relaxation as the transition is initiated. The t/G value drops to 0.016 as post-perovskite is formed at 26.1 GPa and 1013 K. Upon further compression to 29.6 GPa at 1003 K, t/G in post-perovskite increases to 0.020.

Texture development during the experiment is shown as inverse pole figures of the compression direction (Fig. 5). In the perovskite phase we observe a weak maximum at 100 (2.2 mrd) after the closure of the sample chamber (Fig. 5a). As compression of NaCoF₃ continues the maximum at 100 strengthens to an mrd value of 4.2 at 7.3 GPa (Fig. 5b). Upon

further compression to 13.4 GPa, a weak secondary maximum appears at 001 (Fig. 5c). This texture weakens before transitioning to post-perovskite at 26.1 GPa (Fig. 5f). This is likely a feature of the transformation. In all cases, there is a clear minimum at 010 in the perovskite phase.

At 26.1 GPa NaCoF₃ has transformed to a post-perovskite structure, and a weak preferred orientation can be observed at 010 (Fig. 5f). This texture strengthens upon compression to 29.6 GPa with mrd values never exceeding 3. Additionally, a clear minimum at 001 develops upon compression of the post-perovskite phase, as well as a small shift of 010 towards 001 (Fig. 5g).

4 Plastic deformation of NaCoF₃

4.1 Compression textures in NaCoF₃ perovskite

Texture evolution is indicative of ongoing plastic deformation and most likely dislocation glide or twinning. Other deformation mechanisms including dislocation climb or diffusion could be active during deformation; however, these mechanisms would not result in strong deformation textures like those observed in our experiments. In earth sciences, deformation textures in perovskite-structured materials are motivated because the most abundant mineral in the Earth's lower mantle is bridgmanite; (Mg,Fe)SiO₃ in the perovskite structure (Tschauner et al., 2014). Numerous studies have hence addressed the deformation textures and mechanisms in bridgmanite (e.g., Wang et al., 1992; Merkel et al., 2003; Wenk et al., 2004a; Cordier et al., 2004; Wenk et al., 2006; Ferré et al., 2007; Mainprice et al., 2008; Miyagi and Wenk, 2016; Kraych et al., 2016; Boioli et al., 2017). In addition, other studies implement structural analogue compositions such as CaIrO₃ (Niwa et al., 2007), NaMgF₃ (Kaercher et al., 2016), and CaGeO₃ (Wang et al., 2013) as lower pressures and temperatures are required to generate a compression texture, and data are easier to interpret. Furthermore, compression textures in NaCoF₃ have not been investigated before, which only allows us to compare them to other analogues such as the ones mentioned above. It is important to note, however, that not all perovskite-structured materials behave in the same manner during plastic deformation.

Here, we measure compression textures in NaCoF₃ between 1.1 and 29.6 GPa at temperatures between 767 and 1013 K. We observe a 100 compression texture very early in the compression (Fig. 5a) which strengthens with further compression to 18.1 GPa (Fig. 5d). This increase of the 100 texture maximum is accompanied by a decrease in intensity at 010. At 13.4 GPa, we observe the appearance of a secondary maximum at 001. The 100 maximum induced by the first stage of compression compares favorably with experiments on bridgmanite (Merkel et al., 2003; Wenk et al., 2004b; Miyagi and Wenk, 2016) in which it was assigned to a likely contribution of {110} mechanical twinning as iden-

tified in early transmission electron microscope (TEM) studies (Wang et al., 1992). This same 100 texture maximum was also observed in compressed NaMgF₃ (Kaercher et al., 2016). The secondary 001 maximum observed later in compression was also observed in D-DIA deformation experiments on NaMgF₃ (Kaercher et al., 2016) and was reported in the study of Miyagi and Wenk (2016) on bridgmanite at pressures below 55 GPa in which it was assigned to slip along (001).

Based on texture measurements, NaCoF₃ is a good analogue for constraining the plasticity of bridgmanite as both maxima at 100 and 001 are observed in both phases in compression experiments. The interpretation of which deformation mechanisms are responsible for experimental texture, however, requires a comparison with polycrystal plasticity simulations. This allows the most relevant deformation mechanism controlling microstructures in the experiment to be extracted and will be described in Sect. 4.3.

4.2 Compression textures in NaCoF₃ post-perovskite

Texture in post-perovskite can arise from phase transformations (Okada et al., 2010; Miyagi et al., 2010, 2011; Dobson et al., 2013; Miyagi and Wenk, 2016) or plastic deformation (Merkel et al., 2006, 2007; Yamazaki et al., 2006; Niwa et al., 2007; Miyajima and Walte, 2009; Hunt et al., 2016). Here, we measure textures in NaCoF₃ post-perovskite between 26.1 and 29.6 GPa at \approx 1000 K. Post-perovskite is compressed over a restricted pressure range (\approx 4 GPa), little texture evolution is observed, and textures are interpreted to arise primarily from transformation. There is a clear effect of transformation textures vs. deformation textures, and our observed texture mostly results from the phase transformation; thus interpretation based on deformation mechanisms will be biased. For this reason, we will focus on the analysis of the perovskite to post-perovskite transformation in Sect. 5.

4.3 Plastic deformation mechanism in perovskite

Texture development depends on a number of factors including deformation geometry, total strain, starting texture, and plastic deformation mechanism activity. Interpretations can be made by using a visco-plastic self-consistent (VPSC) model, which simulates the plastic deformation of polycrystalline aggregates depending on deformation mechanisms and loading conditions (Wenk, 1999). VPSC modeling has been used in the past to investigate deformation of perovskites at lower-mantle conditions (Mainprice et al., 2008; Miyagi and Wenk, 2016; Kaercher et al., 2016). Based on these publications, we test the following deformation mechanisms, (100)[010], (100)[001], (100)⟨011⟩, (010)[100], (010)⟨101⟩, (001)[100], (001)⟨110⟩, {111}⟨110⟩, and {110}⟨110⟩ twins, in order to generate the best fit texture observed in our experiments (Fig. 5). The final models used are shown in Table 2 and will be described below.

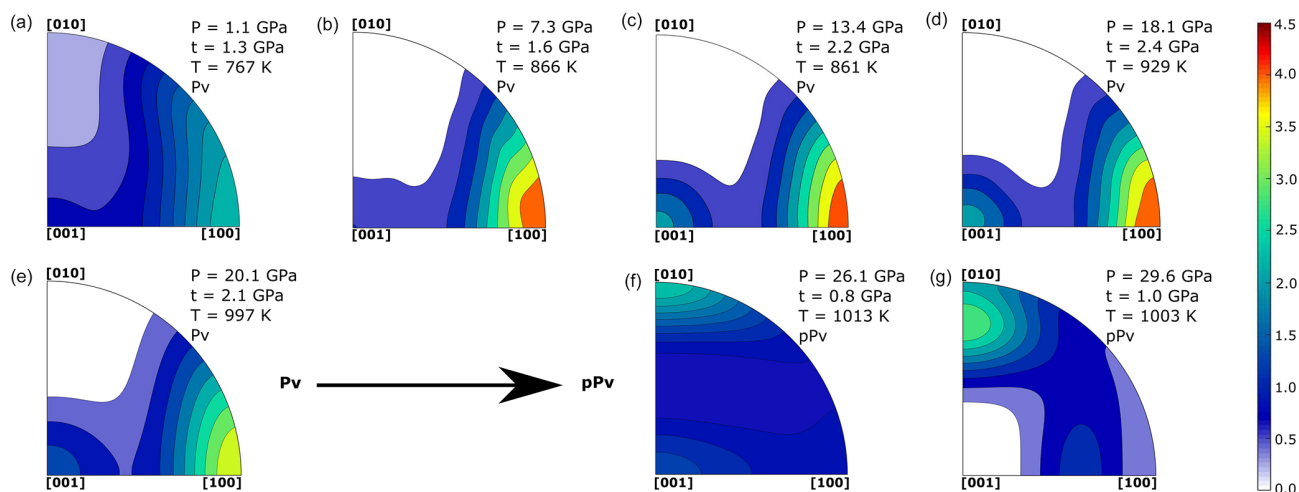


Figure 5. Inverse pole figures in the compression direction of NaCoF₃ at various stages of compression. (a, b, c, d, e) Perovskite structure (Pbmn setting). (f, g) Post-perovskite structure. Equal area projection. Color scale in multiples of random distribution (mrd). Values of *t* reported in the figure assume constant shear modulus value of *G* = 44 GPa.

Table 2. CRSS, start activity, and end activity of slip systems from VPSC calculations for perovskite. Sample compression is modeled in two stages. See text for details.

Slip system	Stage 1 (25 % strain)			Stage 2 (40 % strain)		
	CRSS	Start activity	End activity	CRSS	Start activity	End activity
(100)[010]	3	9.9 %	10.8 %	5	8.4 %	5.1 %
(100)[001]	2	10.2 %	17.8 %	5	0.7 %	1.0 %
(100)(011)	2	32.3 %	44.3 %	5	5.8 %	4.3 %
(010)[100]	5	2.1 %	2.3 %	5	8.4 %	5.1 %
(010)(101)	5	11.5 %	6.8 %	5	3.3 %	2.0 %
(001)[100]	5	0.7 %	1.1 %	6	0.4 %	1.0 %
(001)[010]	5	7.5 %	3.7 %	6	0.0 %	0.0 %
(001)(110)	5	7.5 %	5.2 %	1	69.5 %	79.7 %
{111}(110)	30	1.4 %	7.4 %	30	3.4 %	2.4 %
{110}(110) twin	2	17.0 %	0.5 %	25	0.0 %	0.0 %

The critical resolved shear stress (CRSS) values reported in this paper are only relative values to one another. Due to the absence of single crystal elastic information on NaCoF₃, we lack the elasticity information required to model deformation textures using an elasto-visco-plastic self-consistent (E-VPSC) model which would take into account elastic properties and absolute shear stresses. As a result, we use the visco-plastic self-consistent (VPSC) approach which does not include any effect of elasticity in which we adjust relative CRSS values to best match our observed textures. Starting from a set of 3000 random orientations (Fig. 6a), we can successfully generate a strong 100 texture while depleting 010 and maintaining orientations at 001, as measured at 7.3 GPa (Fig. 5b), by applying 25 % strain in axial compression with dominant slip on (100) and a significant contribution of {110} twins (Fig. 6c). It is necessary to include {110} twins in order to deplete the 010 direction while maintaining orientations at

001. Indeed, dominant slip on (100) only results in the depletion of both 010 and 001 (Kaercher et al., 2016) and is not consistent with our experimental results.

We were then unable to obtain orientations on the secondary 001 maximum while preserving the initial 100 texture as measured in the experiment above 13.4 GPa (Fig. 5c). Among the proposed deformation mechanisms, slip on (001) can indeed move orientations from 100 to 001, but such simulations will generate a slow movement of orientations from 100 to 001, as shown in the second stage simulations (Fig. 6d and e). This is not observed in the experiments for which the 001 maximum increases in the absence of intermediate orientations between 100 and 001. Twinning is an efficient mode for inducing fast grain reorientations without producing a gradual texture shift. The fast reorientation of grains from 100 to 001 hence alludes to a potential contribution of an unknown twinning mode. Despite all our attempts, we were

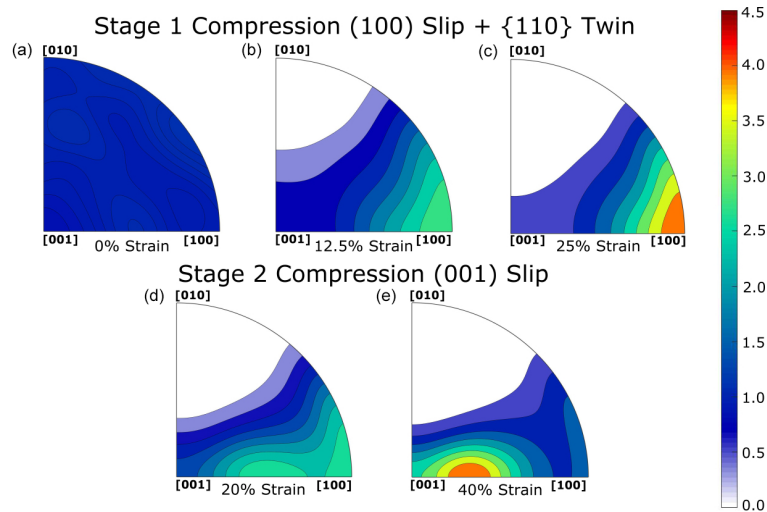


Figure 6. Inverse pole figures (a, b, c) of first stage compression in VPSC simulation starting from a random texture at 0 % strain to 25 % strain dominated by slip along (100) planes with significant contribution of {110} twins. Second stage of deformation (d, e) starting from (c), allowing 20 % and 40 % strain with deformation dominated by (001) slip.

unable to characterize the observed 001 maximum based on twinning laws reported for perovskites.

5 Transformation of perovskite to post-perovskite in NaCoF₃

Many questions have arisen regarding the transformation of perovskite to post-perovskite, including the transformation mechanism itself (Tsuchiya et al., 2004; Oganov et al., 2005; Dobson et al., 2013), its effect on lattice preferred orientations (Okada et al., 2010; Miyagi et al., 2011), stress (Hunt et al., 2009; Dobson et al., 2012), and anisotropy in the Earth's lower mantle (Dobson et al., 2013; Walker et al., 2018b).

5.1 Pressure

Transformation of NaCoF₃ perovskite to post-perovskite takes place between 20.1 and 26.1 GPa. The broad pressure range of conversion reported can be explained by significant peak overlap between perovskite and post-perovskite obscuring the phase transition. We observed the phase transition at higher pressures than Dobson et al. (2011) and Yusa et al. (2012), who observe the transition from perovskite to post-perovskite at 18 GPa and 973 K and 14.5 GPa at 1173 K, respectively. This could be an effect of either stress or kinetics. During our experiment we do not allow as much time at the transition pressure as Dobson et al. (2011) who induced the transformation in a multi-anvil press. Additionally, Yusa et al. (2012) observe disproportionation phases after laser heating above 21 GPa at 1100 K that we do not. This could potentially be explained by the overall lower temperatures in our experiment.

5.2 Stress

With the transition of perovskite to post-perovskite we measure a drop of normalized stress from 0.054 to 0.016 (a factor of 3). In comparison, studies by Hunt et al. (2009) and Dobson et al. (2012) indicate post-perovskite deforms 5 to 10 times faster than perovskite when using analogues NaCoF₃ and CaIrO₃ based on strain rate measurements. Additionally, numerical simulations of diffusion in MgSiO₃ by Ammann et al. (2010) predicted a significantly weaker post-perovskite phase. The observed normalized strength drop in NaCoF₃ upon its transformation to post-perovskite is likely a result of transformation plasticity or transient weakening. In the absence of known values for elastic properties of NaCoF₃ under high P/T , we are unable to report actual differential stress values. Despite this limitation, overall our results are consistent with a weakening of materials at the perovskite to post-perovskite transition.

5.3 Mechanism

Phase transformations change crystal structures but also induce a change in texture of materials. Transformations can be diffusionless in nature, meaning the atoms within the material move in a homogeneous fashion or they can be reconstructive in nature and move by means of long-range diffusion. Diffusionless transformations involve orientation relationships between the parent and daughter phase and are sometimes referred to as martensitic (Christian et al., 1995). Diffusive transformations, on the other hand, do not imply orientation relationships between the parent and daughter phase.

Early predictions by Tsuchiya et al. (2004) indicate that the perovskite to post-perovskite transformation should lead

to orientation relationships. They determine that $[1\bar{1}0]$, $[110]$, and $[001]$ of Pbnm perovskite correspond to $[100]$, $[010]$, and $[001]$, respectively, in Cmcn post-perovskite. In parallel, based on metadynamics, the simulations of Oganov et al. (2005) predict a less cooperative mechanism with stacking faults producing shear and fragments of post-perovskite structures. Experimentally, Dobson et al. (2013) studied the perovskite to post-perovskite transition in NaNiF₃ based on high-pressure experiments and electron microscopy on the recovered samples. They indicate that the *c* axis of the perovskite phase is preserved during the transformation to post-perovskite. In addition, they observed that the post-perovskite *hh0* vector in reciprocal space is parallel to $[010]$ in perovskite.

Here, we test these three different transformation models. The orientation relationships of Tsuchiya et al. (2004), starting from NaCoF₃ perovskite at 20.1 GPa, result in a transformation texture with diffuse weak maximums between 010 and 100 (Fig. 7c). The model proposed by Oganov et al. (2005) is not consistent with our data because orientation relationships are only considered along the *c* direction. We clearly observe a 010 texture in post-perovskite, implying there are additional orientation relationships than that along the *c* direction. When using the orientations relationships in Dobson et al. (2013), the simulated post-perovskite texture matches that measured experimentally (Fig. 7d). In both the experimental and simulated textures, we observe a maximum at 010. Moreover, the strength of the texture is consistent between experiments and simulations.

Based on the above reasoning, we can conclude that the transformation from perovskite to post-perovskite in NaCoF₃ involves orientation relationships and hence falls within the group of displacive phase transformations. Furthermore, these relationships fit the model of Dobson et al. (2013), based on experiments performed on NaNiF₃. This supports the idea that this mechanism could apply to natural perovskite phases.

6 Conclusion

This paper presented experimental results of NaCoF₃ compressed inside a resistive-heated radial diffraction DAC at pressures of 1.1 to 29.6 GPa and temperatures between 300 and 1013 K. A phase transformation from NaCoF₃ perovskite to post-perovskite was observed between 20.1 and 26.1 GPa.

Deformation of NaCoF₃ perovskite initially results in a strong 100 maximum when the sample is at 7.3 GPa. VPSC simulations show that this texture is formed by slip along (100) paired with important contributions from $\{110\}$ twins. Later in the deformation process we observe a weak secondary 001 maximum appearing at 13.4 GPa. These deformation textures are similar to those of NaMgF₃ shown in Kaercher et al. (2016). We attempt to model this secondary

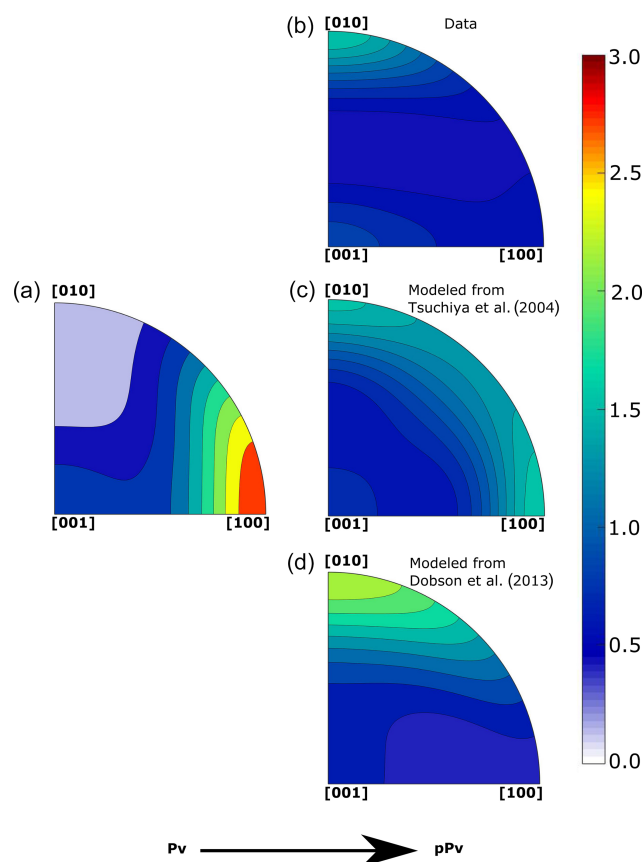


Figure 7. (a) Perovskite texture at 20.1 GPa immediately before transformation to post-perovskite. (b) Post-perovskite texture at 26.1 GPa after transformation from experimental measurements. (c) Modeled transformation texture of post-perovskite using orientation relationships from Tsuchiya et al. (2004). (d) Modeled transformation texture of post-perovskite using orientation relationships from Dobson et al. (2013).

maximum; however, we are unable to recreate it without shifting the original 100 maximum. Such fast grain reorientation could be explained by a twinning mode different from known perovskite twinning modes (Wang et al., 1992). Direct comparisons to MgSiO₃ deformation textures are made difficult because of the effect of starting material on the MgSiO₃ transformation textures (Miyagi and Wenk, 2016). Nevertheless, both the 100 and 001 compression textures observed in NaCoF₃ have been observed in natural compositions (Merkel et al., 2003; Wenk et al., 2004b; Miyagi and Wenk, 2016; Couper et al., 2020). NaCoF₃ hence appears as a good analogue for plasticity studies relevant for the Earth's mantle.

The phase transition from perovskite to post-perovskite results in a normalized strength drop from 0.054 to 0.016 (a factor of 3), which is likely a result of transformation plasticity or transient weakening. Transformation of NaCoF₃ perovskite to post-perovskite is martensitic in nature as demonstrated by the existence of orientation relationships between

both phases. The orientation relationships proposed by Dobson et al. (2013) can successfully reproduce our data.

Perovskite analogues continue to provide valuable insight to the behavior of materials at extreme pressures and temperatures relevant for planetary mantles. For Earth's mantle materials, it is important to understand the effect of temperature on deformation mechanisms which may be different from what is observed at 300 K. Analogues such as NaCoF₃ allow for studies at lower pressures. It would be interesting to study the effect of temperatures at these lower pressures to constrain the effect of temperature on the plasticity of perovskite phases. Further studies on analogues might also include the investigation of post-perovskite deformation textures in NaCoF₃ and other analogues, as well as potential post-post-perovskite phases (Crichton et al., 2016; Umemoto and Wentzcovitch, 2019). A general understanding of plasticity in perovskite and post-perovskite will help with improving the interpretation of seismic models in terms of mantle dynamics such as heat transfer through convection.

Code and data availability. The data were processed using MAUD (<http://maud.radiographema.eu>, Lutterotti et al., 1997) and MTEX (<https://mtex-toolbox.github.io>, Bachmann et al., 2010) which are open source and freely available. VPSC modeling was performed using the Los Alamos visco-plastic self-consistent code available from Ricardo A. Lebensohn and Carlos N. Tomé. Maud and VPSC input files are available on Zenodo using the following link: <https://doi.org/10.5281/zenodo.5513910> (Gay et al., 2021).

Author contributions. LM and SM designed the project. LM, SM, CL, SC, and HPL conducted the experiment. DPD provided the sample. JPG and SM processed and interpreted the data. JPG and SM wrote the paper with comments from LM, SC, DPD, and HPL.

Competing interests. The contact author has declared that neither they nor their co-authors have any competing interests

Disclaimer. Publisher's note: Copernicus Publications remains neutral with regard to jurisdictional claims in published maps and institutional affiliations.

Special issue statement. This article is part of the special issue "Probing the Earth: experiments and mineral physics at mantle depths". It is a result of the 17th International Symposium on Experimental Mineralogy, Petrology and Geochemistry, Potsdam, Germany, 21–24 June 2020.

Acknowledgements. The Chevreul Institute is thanked for its help in the development of this work through the ARCHI-CM project supported by the "Ministère de l'Enseignement Supérieur de la Recherche et de l'Innovation", the region "Hauts-de-France", the

ERDF program of the European Union, and the "Métropole Européenne de Lille". This research was carried out at the P02.2 beamline of the PETRA III synchrotron at DESY, a member of the Helmholtz Association (HGF). The authors would also like to thank Feng Lin for assistance with VPSC modeling.

Financial support. This research has been supported by the Association Nationale de la Recherche et de la Technologie (TIMELESS, grant no. ANR-17-CE31-0025) and the Deutsche Forschungsgemeinschaft (grant nos. TH 1530/18-1, SA 2585/3-1, and SP1216/8-1). It was also supported by the bilateral PROCOPE-PPP program (grant nos. PHC 40555PC and DAAD 57390184). Christopher Langrand also received support from a fellowship of the Université de Lille and the Région Hauts-de-France. The research leading to this result has been supported by the EU Framework Programme for Research and Innovation HORIZON 2020 (CALIPSOplus (grant no. 730872)).

Review statement. This paper was edited by Max Wilke and reviewed by two anonymous referees.

References

- Ammann, M. W., Brodholt, J. P., Wookey, J., and Dobson, D. P.: First-principles constraints on diffusion in lower-mantle minerals and a weak D'' layer, *Nature*, 465, 462–465, <https://doi.org/10.1038/nature09052>, 2010.
- Bachmann, F., Hielscher, R., and Schaeben, H.: Solid State Phenomena, Texture Analysis with MTEX – Free and Open Source Software Toolbox, 160, 63–68, <https://doi.org/10.4028/www.scientific.net/SSP.160.63> (last access 21 September 2021) 2010 (code available at: <https://mtex-toolbox.github.io>, last access: 21 September 2021).
- Beghein, C., Trampert, J., and van Heijst, H. J.: Radial anisotropy in seismic reference models of the mantle, *J. Geophys. Res.-Sol. Ea.*, 111, B02303, <https://doi.org/10.1029/2005JB003728>, 2006.
- Boioli, F., Carrez, P., Cordier, P., Devincere, B., Gouriet, K., Hirel, P., Kraych, A., and Ritterbex, S.: Pure climb creep mechanism drives flow in Earth's lower mantle, *Science Advances*, 3, 1–7, <https://doi.org/10.1126/sciadv.1601958>, 2017.
- Carrez, P., Ferré, D., and Cordier, P.: Implications for plastic flow in the deep mantle from modelling dislocations in MgSiO₃ minerals, *Nature*, 446, 68–70, <https://doi.org/10.1038/nature05593>, 2007.
- Carrez, P., Goryaeva, A. M., and Cordier, P.: Prediction of Mechanical Twinning in Magnesium Silicate Post-Perovskite, *Sci. Rep.*, 7, 17640, <https://doi.org/10.1038/s41598-017-18018-1>, 2017.
- Chen, G., Liebermann, R. C., and Weidner, D. J.: Elasticity of single-crystal MgO to 8 Gigapascals and 1600 Kelvin, *Science*, 280, 1913–1916, <https://doi.org/10.1126/science.280.5371.1913>, 1998.
- Chenine, D., Aziz, Z., Benstaali, W., Bouadjemi, B., Youb, O., Lantri, T., Abbar, B., and Bentata, S.: Theoretical Investigation of Half-Metallic Ferromagnetism in Sodium-Based Fluoroperovskite NaXF₃ (X = V, Co), *J. Supercond. Nov. Magn.*, 31, 285–295, <https://doi.org/10.1007/s10948-017-4204-4>, 2018.

- Christian, J. W., Olson, G. B., and Cohen, M.: Classification of Displacive Transformations: What is a Martensitic Transformation?, *J. Phys. IV France*, 05, C8-3–C8-10, <https://doi.org/10.1051/jp4:1995801>, 1995.
- Čížková, H., Čadek, O., Matyska, C., and Yuen, D. A.: Implications of post-perovskite transport properties for core-mantle dynamics, *Phys. Earth Planet. In.*, 180, 235–243, <https://doi.org/10.1016/j.pepi.2009.08.008>, 2010.
- Cobden, L., Thomas, C., and Trampert, J.: The earth's heterogeneous mantle: A geophysical, geodynamical, and geochemical perspective, Springer International Publishing Switzerland, Cham, Switzerland, https://doi.org/10.1007/978-3-319-15627-9_13, 2015.
- Cordier, P., Ungár, T., Zsoldos, L., and Tichy, G.: Dislocation creep in MgSiO₃ perovskite at conditions of the Earth's uppermost lower mantle, *Nature*, 428, 837–840, <https://doi.org/10.1038/nature02472>, 2004.
- Couper, S., Speziale, S., Marquardt, H., Liermann, H. P., and Miyagi, L.: Does Heterogeneous Strain Act as a Control on Seismic Anisotropy in Earth's Lower Mantle?, *Front. Earth Sci.*, 8, 540449, <https://doi.org/10.3389/feart.2020.540449>, 2020.
- Crichton, W., Bernal, F., Guignard, J., Hanfland, M., and Margadonna, S.: Observation of Sb₂S₃-type post-post-perovskite in NaFeF₃. Implications for ABX₃ and A₂X₃ systems at ultrahigh pressure, *Mineral. Mag.*, 80, 659–674, 2016.
- Dobson, D. P., Hunt, S. A., Lindsay-Scott, A., and Wood, I. G.: Towards better analogues for MgSiO₃ post-perovskite: NaCoF₃ and NaNiF₃, two new recoverable fluoride post-perovskites, *Phys. Earth Planet. In.*, 189, 171–175, <https://doi.org/10.1016/j.pepi.2011.08.010>, 2011.
- Dobson, D. P., McCormack, R., Hunt, S. A., Ammann, M. W., Weidner, D., Li, L., and Wang, L.: The relative strength of perovskite and post-perovskite NaCoF₃, *Mineral. Mag.*, 76, 925–932, <https://doi.org/10.1180/minmag.2012.076.4.09>, 2012.
- Dobson, D. P., Miyajima, N., Nestola, F., Alvaro, M., Casati, N., Liebske, C., Wood, I. G., and Walker, A. M.: Strong inheritance of texture between perovskite and post-perovskite in the D'' layer, *Nat. Geosci.*, 6, 575–578, <https://doi.org/10.1038/ngeo1844>, 2013.
- Dorfman, S. M., Shieh, S. R., and Duffy, T. S.: Strength and texture of Pt compressed to 63 GPa, *J. Appl. Phys.*, 117, 065901, <https://doi.org/10.1063/1.4907866>, 2015.
- Duffy, T. S.: Strength of materials under static loading in the diamond anvil cell, *AIP Conf. Proc.*, 955, 639–644, <https://doi.org/10.1063/1.2833175>, 2007.
- Ferré, D., Carrez, P., and Cordier, P.: First principles determination of dislocations properties of MgSiO₃ perovskite at 30 GPa based on the Peierls-Nabarro model, *Phys. Earth Planet. In.*, 163, 283–291, <https://doi.org/10.1016/j.pepi.2007.05.011>, 2007.
- Ferreira, A. M., Faccenda, M., Sturgeon, W., Chang, S. J., and Scharndong, L.: Ubiquitous lower-mantle anisotropy beneath subduction zones, *Nat. Geosci.*, 12, 301–306, <https://doi.org/10.1038/s41561-019-0325-7>, 2019.
- Garnero, E. J., Maupin, V., Lay, T., and Fouch, M. J.: Variable azimuthal anisotropy in earth's lowermost mantle, *Science*, 306, 259–261, <https://doi.org/10.1126/science.1103411>, 2004.
- Gay, J. P., Miyagi, L., Couper, S., Langrand, C., Dobson, D. P., Liermann, H.-P., and Merkel, S.: Data for deformation and transformation of NaCoF₃ perovskite and post-perovskite up to 30 GPa and 1013 K, Zenodo [data set], <https://doi.org/10.5281/zenodo.5513910>, 2021.
- Girard, J., Amulele, G., Farla, R., Mohiuddin, A., and Karato, S. I.: Shear deformation of bridgmanite and magnesiowüstite aggregates at lower mantle conditions, *Science*, 351, 144–147, <https://doi.org/10.1126/science.aad3113>, 2016.
- Gonzalez-Platas, J., Alvaro, M., Nestola, F., and Angel, R.: EosFit7-GUI: A new graphical user interface for equation of state calculations, analyses and teaching, *J. Appl. Crystallogr.*, 49, 1377–1382, <https://doi.org/10.1107/S1600576716008050>, 2016.
- Hernlund, J. W., Thomas, C., and Tackley, P. J.: A doubling of the post-perovskite, *Nature*, 434, 882–886, <https://doi.org/10.1038/nature03472>, 2005.
- Hunt, S. A., Weidner, D. J., Li, L., Wang, L., Walte, N. P., Brodholt, J. P., and Dobson, D. P.: Weakening of calcium iridate during its transformation from perovskite to post-perovskite, *Nat. Geosci.*, 2, 794–797, <https://doi.org/10.1038/ngeo663>, 2009.
- Hunt, S. A., Walker, A. M., and Mariani, E.: In-situ measurement of texture development rate in CaIrO₃ post-perovskite, *Phys. Earth Planet. In.*, 257, 91–104, <https://doi.org/10.1016/j.pepi.2016.05.007>, 2016.
- Immoor, J., Marquardt, H., Miyagi, L., Speziale, S., Merkel, S., Schwark, I., Ehnes, A., and Liermann, H.-P.: An improved setup for radial diffraction experiments at high pressures and high temperatures in a resistive graphite-heated diamond anvil cell, *Rev. Sci. Instrum.*, 91, 045121, <https://doi.org/10.1063/1.5143293>, 2020.
- Kaercher, P., Miyagi, L., Kanitpanyacharoen, W., Zepeda-Alarcon, E., Wang, Y., Parkinson, D., Lebensohn, R. A., De Carlo, F., and Wenk, H. R.: Two-phase deformation of lower mantle mineral analogs, *Earth Planet. Sc. Lett.*, 456, 134–145, <https://doi.org/10.1016/j.epsl.2016.09.030>, 2016.
- Koelmeijer, P., Schuberth, B. S., Davies, D. R., Deuss, A., and Ritsema, J.: Constraints on the presence of post-perovskite in Earth's lowermost mantle from tomographic-geodynamic model comparisons, *Earth Planet. Sc. Lett.*, 494, 226–238, <https://doi.org/10.1016/j.epsl.2018.04.056>, 2018.
- Kraych, A., Carrez, P., and Cordier, P.: On dislocation glide in MgSiO₃ bridgmanite at high-pressure and high-temperature, *Earth Planet. Sc. Lett.*, 452, 60–68, <https://doi.org/10.1016/j.epsl.2016.07.035>, 2016.
- Liermann, H.-P., Merkel, S., Miyagi, L., Wenk, H.-R., Shen, G., Cynn, H., and Evans, W. J.: Experimental method for in situ determination of material textures at simultaneous high pressure and high temperature by means of radial diffraction in the diamond anvil cell, *Rev. Sci. Instrum.*, 80, 104501, <https://doi.org/10.1063/1.3236365>, 2009.
- Liermann, H.-P., Konôpková, Z., Morgenroth, W., Glazyrin, K., Bednarcik, J., McBride, E. E., Petitgirard, S., Delitz, J. T., Wendt, M., Bican, Y., Ehnes, A., Schwark, I., Rothkirch, A., Tischer, M., Heuer, J., Schulte-Schrepping, H., Kracht, T., and Franz, H.: The Extreme Conditions Beamline P02.2 and the Extreme Conditions Science Infrastructure at PETRA III, *J. Synchrotron Radiat.*, 22, 908–924, <https://doi.org/10.1107/S1600577515005937>, 2015.
- Lutterotti, L., Matthies, S., Wenk, H. R., Schultz, A. S., and Richardson, J. W.: Combined texture and structure analysis of deformed limestone from time-of-flight neutron diffraction spectra, *J. Appl. Phys.*, 81, 594–600, <https://doi.org/10.1063/1.364220>,

- 1997 (data available at: <http://maud.radiographema.eu>, last access: 17 September 2021).
- Mainprice, D., Barruol, G., Isma, W. B., Mainprice, D., Barruol, G., Isma, W. B., Mainprice, D., Barruol, G., and Isma, W. B.: The Seismic anisotropy of the Earth's mantle: From single crystal to polycrystal, vol. 117, American Geophysical Union, Washington D.C., USA, <https://doi.org/10.1029/GM117>, 2000.
- Mainprice, D., Tommasi, A., Ferré, D., Carrez, P., and Cordier, P.: Predicted glide systems and crystal preferred orientations of polycrystalline silicate Mg-Perovskite at high pressure: Implications for the seismic anisotropy in the lower mantle, *Earth Planet. Sc. Lett.*, 271, 135–144, <https://doi.org/10.1016/j.epsl.2008.03.058>, 2008.
- McCormack, R., Dobson, D. P., Walte, N. P., Miyajima, N., Taniguchi, T., and Wood, I. G.: The development of shape- and crystallographic-preferred orientation in CaPtO₃ post-perovskite deformed in pure shear, *Am. Mineral.*, 96, 1630–1635, <https://doi.org/10.2138/am.2011.3881>, 2011.
- Merkel, S., Wenk, H. R., Badro, J., Montagnac, G., Gillet, P., Mao, H. K., and Hemley, R. J.: Deformation of (Mg_{0.9}Fe_{0.1})SiO₃ Perovskite aggregates up to 32 GPa, *Earth Planet. Sc. Lett.*, 209, 351–360, [https://doi.org/10.1016/S0012-821X\(03\)00098-0](https://doi.org/10.1016/S0012-821X(03)00098-0), 2003.
- Merkel, S., Kubo, A., Miyagi, L., Speziale, S., Duffy, T. S., Mao, H. K., and Wenk, H. R.: Plastic deformation of MgGeO₃ post-perovskite at lower mantle pressures, *Science*, 311, 644–646, <https://doi.org/10.1126/science.1121808>, 2006.
- Merkel, S., McNamara, A. K., Kubo, A., Speziale, S., Miyagi, L., Meng, Y., Duffy, T. S., and Wenk, H. R.: Deformation of (Mg,Fe)SiO₃ post-perovskite and D'' anisotropy, *Science*, 316, 1729–1732, <https://doi.org/10.1126/science.1140609>, 2007.
- Metsue, A., Carrez, P., Mainprice, D., and Cordier, P.: Numerical modelling of dislocations and deformation mechanisms in CaIrO₃ and MgGeO₃ post-perovskites – Comparison with MgSiO₃ post-perovskite, *Phys. Earth Planet. In.*, 174, 165–173, <https://doi.org/10.1016/j.pepi.2008.04.003>, 2009.
- Miyagi, L. and Wenk, H. R.: Texture development and slip systems in bridgmanite and bridgmanite + ferropericlase aggregates, *Phys. Chem. Miner.*, 43, 597–613, <https://doi.org/10.1007/s00269-016-0820-y>, 2016.
- Miyagi, L., Nishiyama, N., Wang, Y., Kubo, A., West, D. V., Cava, R. J., Duffy, T. S., and Wenk, H. R.: Deformation and texture development in CaIrO₃ post-perovskite phase up to 6 GPa and 1300 K, *Earth Planet. Sc. Lett.*, 268, 515–525, <https://doi.org/10.1016/j.epsl.2008.02.005>, 2008.
- Miyagi, L., Merkel, S., Yagi, T., Sata, N., Ohishi, Y., and Wenk, H. R.: Diamond anvil cell deformation of CaSiO₃ perovskite up to 49 GPa, *Phys. Earth Planet. In.*, 174, 159–164, <https://doi.org/10.1016/j.pepi.2008.05.018>, 2009.
- Miyagi, L., Kanitpanyacharoen, W., Kaercher, P., Lee, K. K., and Wenk, H. R.: Slip systems in MgSiO₃ post-perovskite: Implications for D'' anisotropy, *Science*, 329, 1639–1641, <https://doi.org/10.1126/science.1192465>, 2010.
- Miyagi, L., Kanitpanyacharoen, W., Stackhouse, S., Militzer, B., and Wenk, H. R.: The enigma of post-perovskite anisotropy: Deformation versus transformation textures, *Phys. Chem. Miner.*, 38, 665–678, <https://doi.org/10.1007/s00269-011-0439-y>, 2011.
- Miyagi, L., Kanitpanyacharoen, W., Raju, S. V., Kaercher, P., Knight, J., MacDowell, A., Wenk, H. R., Williams, Q., and Alarcon, E. Z.: Combined resistive and laser heating technique for in situ radial X-ray diffraction in the diamond anvil cell at high pressure and temperature, *Rev. Sci. Instrum.*, 84, 025118, <https://doi.org/10.1063/1.4793398>, 2013.
- Miyajima, N. and Walte, N.: Burgers vector determination in deformed perovskite and post-perovskite of CaIrO₃ using thickness fringes in weak-beam dark-field images, *Ultramicroscopy*, 109, 683–692, <https://doi.org/10.1016/j.ultramic.2009.01.010>, 2009.
- Murakami, M., Hirose, K., Kawamura, K., Sata, N., and Ohishi, Y.: Post-Perovskite Phase Transition in MgSiO₃, *Science*, 304, 855–858, <https://doi.org/10.1126/science.1095932>, 2004.
- Nakagawa, T. and Tackley, P. J.: Effects of low-viscosity post-perovskite on thermo-chemical mantle convection in a 3-D spherical shell, *Geophys. Res. Lett.*, 38, L04309, <https://doi.org/10.1029/2010GL046494>, 2011.
- Niwa, K., Yagi, T., Ohgushi, K., Merkel, S., Miyajima, N., and Kikegawa, T.: Lattice preferred orientation in CaIrO₃ perovskite and post-perovskite formed by plastic deformation under pressure, *Phys. Chem. Miner.*, 34, 679–686, <https://doi.org/10.1007/s00269-007-0182-6>, 2007.
- Nowacki, A., Wookey, J., and Kendall, J. M.: Deformation of the lowermost mantle from seismic anisotropy, *Nature*, 467, 1091–1094, <https://doi.org/10.1038/nature09507>, 2010.
- Nowacki, A., Walker, A. M., Wookey, J., and Kendall, J. M.: Evaluating post-perovskite as a cause of D'' anisotropy in regions of palaeosubduction, *Geophys. J. Int.*, 192, 1085–1090, <https://doi.org/10.1093/gji/ggs068>, 2013.
- Oganov, A. R. and Ono, S.: Theoretical and experimental evidence for a post-perovskite phase of MgSiO₃ in Earth's D'' layer, *Nature*, 430, 445–448, <https://doi.org/10.1038/nature02701>, 2004.
- Oganov, A. R., Martoňák, R., Laio, A., Raiteri, P., and Parrinello, M.: Anisotropy of earth's D'' layer and stacking faults in the MgSiO₃ post-perovskite phase, *Nature*, 438, 1142–1144, <https://doi.org/10.1038/nature04439>, 2005.
- Okada, T., Yagi, T., Niwa, K., and Kikegawa, T.: Lattice-preferred orientations in post-perovskite-type MgGeO₃ formed by transformations from different pre-phases, *Phys. Earth Planet. In.*, 180, 195–202, <https://doi.org/10.1016/j.pepi.2009.08.002>, 2010.
- Panning, M. and Romanowicz, B.: A three-dimensional radially anisotropic model of shear velocity in the whole mantle, *Geophys. J. Int.*, 167, 361–379, <https://doi.org/10.1111/j.1365-246X.2006.03100.x>, 2006.
- Pisconti, A., Thomas, C., and Wookey, J.: Discriminating Between Causes of D'' Anisotropy Using Reflections and Splitting Measurements for a Single Path, *J. Geophys. Res.-Sol. Ea.*, 124, 4811–4830, <https://doi.org/10.1029/2018JB016993>, 2019.
- Popa, N. C.: The (*hkl*) Dependence of Diffraction-Line Broadening Caused by Strain and Size for all Laue Groups in Rietveld Refinement, *J. Appl. Crystallogr.*, 31, 176–180, <https://doi.org/10.1107/S0021889897009795>, 1998.
- Romanowicz, B. and Wenk, H. R.: Anisotropy in the deep Earth, *Phys. Earth Planet. In.*, 269, 58–90, <https://doi.org/10.1016/j.pepi.2017.05.005>, 2017.
- Savage, M. S.: Seismic anisotropy and mantle deformation: What have we learned from shear wave splitting?, *Rev. Geophys.*, 37, 65–106, <https://doi.org/10.1029/98RG02075>, 1999.
- Shirako, Y., Shi, Y. G., Aimi, A., Mori, D., Kojitani, H., Yamaura, K., Inaguma, Y., and Akaogi, M.: High-pressure stability relations, crystal structures, and physical properties of perovskite and

- post-perovskite of NaNiF₃, *J. Solid State Chem.*, 191, 167–174, <https://doi.org/10.1016/j.jssc.2012.03.004>, 2012.
- Singh, A. K., Balasingh, C., Mao, H. K., Hemley, R. J., and Shu, J.: Analysis of lattice strains measured under nonhydrostatic pressure, *J. Appl. Phys.*, 83, 7567–7575, <https://doi.org/10.1063/1.367872>, 1998.
- Tackley, P. J.: Dynamics and evolution of the deep mantle resulting from thermal, chemical, phase and melting effects, *Earth-Sci. Rev.*, 110, 1–25, <https://doi.org/10.1016/j.earscirev.2011.10.001>, 2012.
- Tschauner, O., Chi, M., Beckett, J. R., Prescher, C., Prakapenka, V. B., and Rossman, G. R.: Discovery of bridgmanite, the most abundant mineral in Earth, in a shocked meteorite, *Science*, 346, 1100–1102, <https://doi.org/10.1126/science.1259369>, 2014.
- Tsuchiya, T., Tsuchiya, J., Umemoto, K., and Wentzcovitch, R. M.: Phase transition in MgSiO₃ perovskite in the earth's lower mantle, *Earth Planet. Sci. Lett.*, 224, 241–248, <https://doi.org/10.1016/j.epsl.2004.05.017>, 2004.
- Tsujino, N., Nishihara, Y., Yamazaki, D., Seto, Y., Higo, Y., and Takahashi, E.: Mantle dynamics inferred from the crystallographic preferred orientation of bridgmanite, *Nature*, 539, 81–84, <https://doi.org/10.1038/nature19777>, 2016.
- Umemoto, K. and Wentzcovitch, R. M.: Ab initio exploration of post-PPV transitions in low-pressure analogs of MgSiO₃, *Physical Review Materials*, 3, 25–28, <https://doi.org/10.1103/PhysRevMaterials.3.123601>, 2019.
- Walker, A. M., Dobson, D. P., Wookey, J., Nowacki, A., and Forte, A. M.: The anisotropic signal of topotaxy during phase transitions in D'', *Phys. Earth Planet. In.*, 276, 159–171, <https://doi.org/10.1016/j.pepi.2017.05.013>, 2018a.
- Walker, A. M., Dobson, D. P., Wookey, J., Nowacki, A., and Forte, A. M.: The anisotropic signal of topotaxy during phase transitions in D'', *Phys. Earth Planet. In.*, 276, 159–171, <https://doi.org/10.1016/j.pepi.2017.05.013>, 2018b.
- Walte, N. P., Heidelberg, F., Miyajima, N., Frost, D. J., Rubie, D. C., and Dobson, D. P.: Transformation textures in post-perovskite: Understanding mantle flow in the D'' layer of the earth, *Geophys. Res. Lett.*, 36, 3–7, <https://doi.org/10.1029/2008GL036840>, 2009.
- Wang, Y., Guyot, F., and Liebermann, R. C.: Electron microscopy of (Mg, Fe)SiO₃ perovskite: evidence for structural phase transitions and implications for the lower mantle, *J. Geophys. Res.*, 97, 327–347, <https://doi.org/10.1029/92jb00870>, 1992.
- Wang, Y., Hilaret, N., Nishiyama, N., Yahata, N., Tsuchiya, T., Morard, G., and Fiquet, G.: High-pressure, high-temperature deformation of CaGeO₃ (perovskite)±MgO aggregates: Implications for multiphase rheology of the lower mantle, *Geochem. Geophys. Geosy.*, 14, 3389–3408, <https://doi.org/10.1002/ggge.20200>, 2013.
- Wenk, H. R.: A voyage through the deformed Earth with the self-consistent model, *Model. Simul. Mater. Sc.*, 7, 699, <http://stacks.iop.org/0965-0393/7/i=5/a=304> (last access: 13 March 2019), 1999.
- Wenk, H. R., Lonardelli, I., Pehl, J., Devine, J., Prakapenka, V., Shen, G., and Mao, H. K.: In situ observation of texture development in olivine, ringwoodite, magnesiowüstite and silicate perovskite at high pressure, *Earth Planet. Sc. Lett.*, 226, 507–519, <https://doi.org/10.1016/j.epsl.2004.07.033>, 2004a.
- Wenk, H. R., Lonardelli, I., Pehl, J., Devine, J., Prakapenka, V., Shen, G., and Mao, H. K.: In situ observation of texture development in olivine, ringwoodite, magnesiowüstite and silicate perovskite at high pressure, *Earth Planet. Sc. Lett.*, 226, 507–519, <https://doi.org/10.1016/j.epsl.2004.07.033>, 2004b.
- Wenk, H. R., Lonardelli, I., Merkel, S., Miyagi, L., Pehl, J., Speziale, S., and Tommaseo, C. E.: Deformation textures produced in diamond anvil experiments, analysed in radial diffraction geometry, *Journal of Physics Condensed Matter*, 18, S933–S947, <https://doi.org/10.1088/0953-8984/18/25/S02>, 2006.
- Wenk, H. R., Lutterotti, L., Kaercher, P., Kanitpanyacharoen, W., Miyagi, L., and Vasin, R.: Rietveld texture analysis from synchrotron diffraction images. II. Complex multiphase materials and diamond anvil cell experiments, *Powder Diffraction*, 29, 220–232, <https://doi.org/10.1017/S0885715614000360>, 2014.
- Wookey, J. and Kendall, J. M.: Seismic Anisotropy of Post-Perovskite and the Lowermost Mantle, 174, 171–189, available at: <https://agupubs.onlinelibrary.wiley.com/doi/10.1029/174GM13> (last access: 23 July 2021), 2007.
- Wookey, J., Kendall, J. M., and Barruol, G.: Mid-mantle deformation inferred from seismic anisotropy, *Nature*, 415, 777–780, <https://doi.org/10.1038/415777a>, 2002.
- Yamazaki, D. and Karato, S. I.: Lattice-Preferred Orientation of Lower Mantle Materials and Seismic Anisotropy in the D'' Layer, Washington DC American Geophysical Union Geophysical Monograph Series, pp. 69–78, available at: <https://agupubs.onlinelibrary.wiley.com/doi/10.1029/174GM07> (last access: 29 July 2021), 2007.
- Yamazaki, D., Yoshino, T., Ohfuji, H., Ando, J.-i., and Yoneda, A.: Origin of seismic anisotropy in the D'' layer inferred from shear deformation experiments on post-perovskite phase, *Earth Planet. Sc. Lett.*, 252, 372–378, <https://doi.org/10.1016/j.epsl.2006.10.004>, 2006.
- Yusa, H., Shirako, Y., Akaogi, M., Kojitani, H., Hirao, N., Ohishi, Y., and Kikegawwa, T.: Perovskite-to-Postperovskite Transitions in NaNiF₃ and NaCoF₃ and Disproportionation of NaCoF₃ Postperovskite under High Pressure and High Temperature, *Inorg. Chem.*, 51, 6559–6566, <https://doi.org/10.1021/ic300118d>, 2012.
- Zha, C. S., Mibe, K., Bassett, W. A., Tschauner, O., Mao, H. K., and Hemley, R. J.: *P-V-T* equation of state of platinum to 80 GPa and 1900 K from internal resistive heating/x-ray diffraction measurements, *J. Appl. Phys.*, 103, 054908, <https://doi.org/10.1063/1.2844358>, 2008.